RESEARCH ARTICLE　　　　　　　　　　　　　　　　　　　　　　**Open Access**

Carbonate clumped isotope thermometry of fault rocks and its possibilities: tectonic implications from calcites within Himalayan Frontal Fold-Thrust Belt

Dyuti Prakash Sarkar[1,2]*, Jun-ichi Ando[1,2], Akihiro Kano[3], Hirokazu Kato[3], Gautam Ghosh[2,4] and Kaushik Das[1,2]

Abstract

Disentangling the temperature and depth of formation of fault rocks is critical for understanding their rheology, exhumation, and the evolution of fault zones. Estimation of fault rock temperatures mostly relies on conventional geothermometers of metamorphic minerals and element partitioning analysis, which are largely inapplicable in shallow crustal fault rocks. Here, we demonstrate the applicability of the carbonate clumped isotope thermometer in low-grade carbonate-bearing fault rocks from the Himalayan frontal wedge (northwest India). Coalescing carbonate clumped isotope thermometry and calcite e-twin morphology allows us to constrain the temperature and depth of formation of the two main thrusts of the Himalayan frontal wedge, the Nahan thrust (170 ± 10 °C; 6–7 km depth), and the Main Boundary thrust (262 ± 30 °C; 10–11 km depth). The integration of the adopted analytical techniques can promote the application of calcite-based clumped isotope thermometry to the fault zone processes and refinement of shallow crustal fault zone models.

1 Introduction

Carbonate clumped isotopes refer to the CO_2 generated by the $CaCO_3$-acid reaction, which contains two or more heavy isotopes like ^{13}C and ^{18}O (Ghosh et al. 2006a). The clumped isotope measurements are represented by mass 47 anomaly (Δ_{47}) in the generated CO_2 gas. The Δ_{47} values, therefore, indicate the abundance anomaly of ^{13}C-^{18}O bonds from the stochastic distribution (Affek and Eiler 2006; Eiler and Schauble 2004; Kluge et al. 2015). The degree to which these heavy isotopes bond to each other depends on rotational and vibrational frequencies of the bonds (Wang et al. 2004) and entropy of the system (Schauble et al. 2006; Swanson et al. 2012) and decreases with increasing temperature (Ryb et al. 2017).

Carbonate clumped isotope (Δ_{47}) thermometry has become a robust technique in the past decade and has been primarily used for carbonates formed in surface environments at temperatures below 35 °C (Eiler 2007; Ghosh et al. 2006a). At about > 100 °C temperatures, initial Δ_{47} values may decrease through solid-state reordering and reflect values characteristic of higher temperature crustal settings (Passey and Henkes 2012; Stolper and Eiler 2015). Existing application of carbonate clumped isotope thermometry addresses queries from a variety of geological settings that include burial in sedimentary basins (Henkes et al. 2014; Shenton et al. 2015), exhumation in orogenic belts (Huntington et al. 2015; Huntington and Lechler 2015; Ryb et al. 2017), and palaeothermometry in low-temperature (< 400 °C) contact and regional metamorphic belts (Ferry et al. 2011; Lloyd et al. 2017). However, the application of Δ_{47} thermometry in calcite-bearing rocks and syn-tectonic veins is limited till date (Lloyd et al. 2017; MacDonald et al. 2019; Siman-Tov et al. 2016; Swanson et al. 2012).

* Correspondence: dpsarkar14@icloud.com
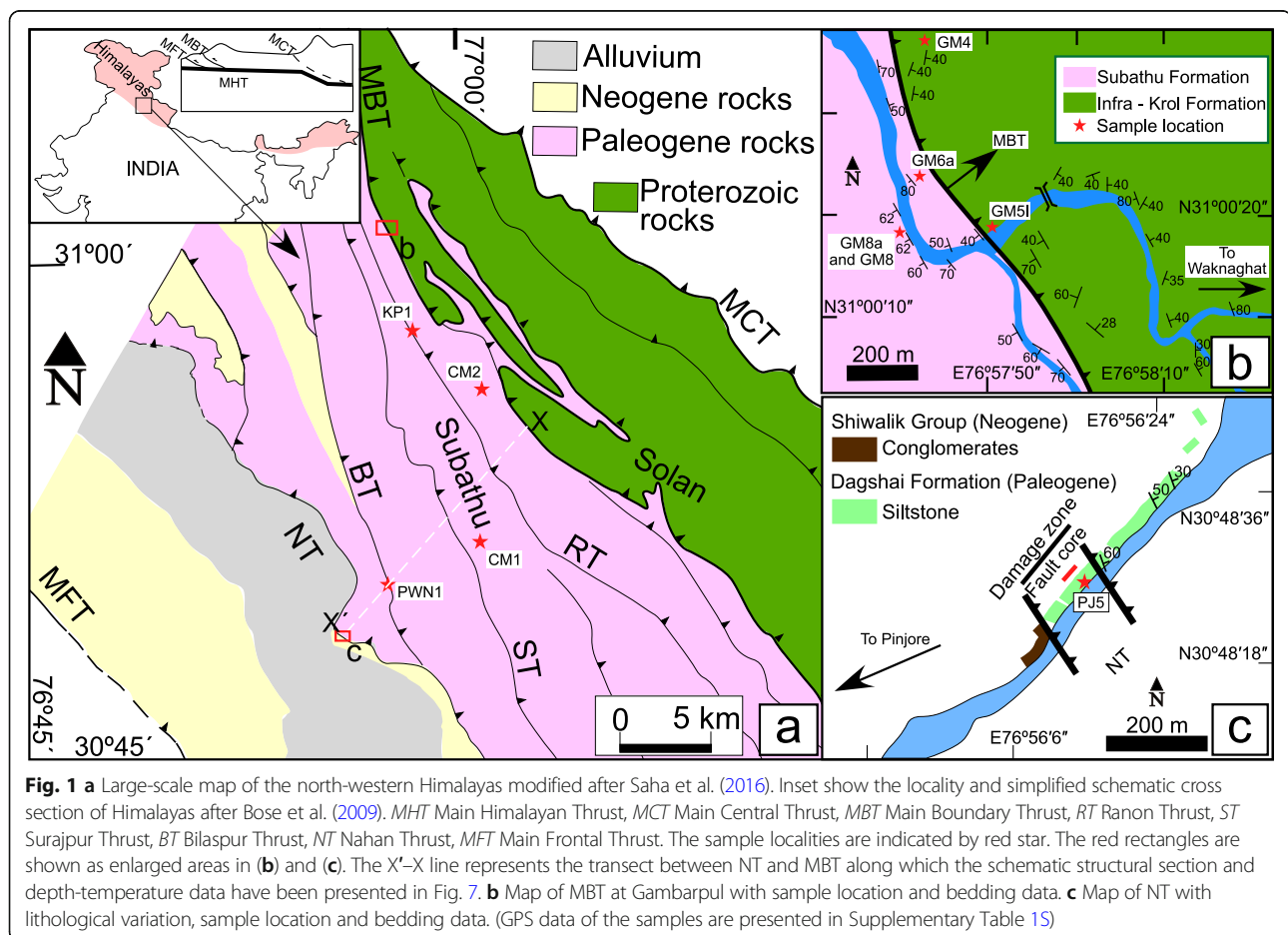[1]Department of Earth and Planetary Systems Science, Hiroshima University, Hiroshima 739-8526, Japan
[2]Hiroshima Institute of Plate Convergence Region Research, Hiroshima University, Hiroshima 739-8526, Japan
Full list of author information is available at the end of the article

Presently, estimation of deformation temperature from low-grade calcite-bearing metamorphic fault rocks relies primarily on the identification and characterization of the deformation twin patterns (Burkhard 1993; Ferrill et al. 2004; Ferrill and Groshong 1993; Rybacki et al. 2013), which is a semi-quantitative technique and provide a range of deformation temperatures. The generation of deformation twins in calcite is grain-size sensitive (Lacombe 2010; Newman 1994; Rybacki et al. 2013) and dependent on the amount of strain hardening (Ferrill et al. 2004; Parlangeau et al. 2019; Rowe and Rutter 1990). In contrast, the Δ_{47} thermometry provides temperature estimation independent of grain size and effects of strain hardening (Ghosh et al. 2006b; Henkes et al. 2013; Schauble et al. 2006) but is dependent on carbonate mineralogy (e.g., calcite, aragonite, or dolomite) that affects the kinetics, closure temperature, and re-ordering of clumped isotopes (Bonifacie et al. 2017; Eiler 2011; Ferry et al. 2011; Stolper and Eiler 2015). Hence, both the techniques independently has certain limitations and must be used with caution.

The present study is focused on syn-tectonic calcite veins and skeletal (bio-clasts) calcite in deformed limestones present within the Himalayan frontal wedge,

bounded between the Nahan thrust (NT) and the Main Boundary Thrust (MBT) (Fig. 1). This study aims to correlate the temperature estimation from deformation microstructures (primarily deformation twins of calcite) with Δ_{47} thermometry, elucidating the deformation temperatures and depth of generation of these fault rocks. This information is crucial to grasp fault behavior at different crustal depths. A large database exists regarding metamorphic mineral growth, P-T-t path, and exhumation rate from the rocks of the Higher Himalayan Sequence (HHS) and the orogenic core (Bollinger et al. 2004; Chakraborty et al. 2017; Chakraborty et al. 2016; Martin 2017; McQuarrie and Ehlers 2015; Schultz et al., 2016; Webb et al. 2011; Yin 2006). In comparison, data on P-T estimates from the MBT, the Sub Himalayan Sequence (SHS), and adjoining thrusts in the frontal fold-thrust belt (FTB) are limited (Mukhopadhyay and Mishra 2005; Sharma et al. 2019; Singh et al. 2015), mainly due to the non-availability of suitable thermometers for these unmetamorphosed to low-grade metamorphosed rocks. Peak metamorphic temperatures not exceeding ~ 330 °C have been reported from the Lesser Himalayan Sequence (LHS) in the MBT hanging wall

Fig. 1 a Large-scale map of the north-western Himalayas modified after Saha et al. (2016). Inset show the locality and simplified schematic cross section of Himalayas after Bose et al. (2009). *MHT* Main Himalayan Thrust, *MCT* Main Central Thrust, *MBT* Main Boundary Thrust, *RT* Ranon Thrust, *ST* Surajpur Thrust, *BT* Bilaspur Thrust, *NT* Nahan Thrust, *MFT* Main Frontal Thrust. The sample localities are indicated by red star. The red rectangles are shown as enlarged areas in (**b**) and (**c**). The X′–X line represents the transect between NT and MBT along which the schematic structural section and depth-temperature data have been presented in Fig. 7. **b** Map of MBT at Gambarpul with sample location and bedding data. **c** Map of NT with lithological variation, sample location and bedding data. (GPS data of the samples are presented in Supplementary Table 1S)

(Célérier et al. 2009; Colleps et al. 2018) from NW Himalaya where at most places these rocks were never buried to temperatures greater than 230–250 °C (Yu 2014). The data and thermal modeling reveal cooling and exhumation initiated at ~ 4–5 Ma in SHS and by ~ 2–4 Ma; it affected the entire SHS (Colleps et al. 2018; Gavillot et al. 2018; Patel and Manmohan 2020). The current study also aims to bridge the gap of thermometric data within SHS, through the amalgamation of calcite twin morphology and clumped isotope studies to provide more accurate estimates of deformation temperatures. It also examines the reliability and applicability of independent usage of Δ_{47} thermometry in estimating deformation temperatures of calcite-bearing unmetamorphosed to low-grade metamorphosed rocks.

2 Geological setting and samples

The Himalayan fold-thrust belt comprises of three main regional thrusts. From north to the south these are the Main Central Thrust (MCT), the Main Boundary Thrust (MBT), and the Main Frontal Thrust (MFT; Fig. 1a), which merge at depth to a single mid-crustal detachment named the Main Himalayan Thrust (MHT; Fig. 1a) (Chemenda et al. 2000; Cottle et al. 2015; Gibbons et al. 2015; Hodges 2000; Martin 2017; Webb et al. 2011; Yin 2006). These regional thrusts separate the major tectonostratigraphic units in the Himalayan belt which, from north to south are the Higher Himalayan Sequence (HHS), the Lesser Himalayan Sequence (LHS), the Sub Himalayan Sequence (SHS), and the Indo-Gangetic alluvium (Yin 2006). A southwest verging forward-propagating thrust sequence has been proposed with sequential emplacement of the MCT at ca. 22–20 Ma (DeCelles et al. 1998; Hodges 2000; Metcalfe 1993; Searle and Godin 2003), the MBT at ca. 11–10 Ma (Burbank et al. 1996; Lavé and Avouac 2000; Meigs et al. 1995; Sangode and Kumar 2003), and the MFT at ~ 2 Ma (Burbank et al. 1996; Kumar et al. 2006; Lavé and Avouac 2000; Meigs et al. 1995; Sangode and Kumar 2003; Sapkota et al. 2013). Thermal models of the age data demonstrate high thrust-related exhumation rates (≥ 1 mm/year) within the SHS (Colleps et al. 2018; Gavillot et al. 2018; Yu 2014), while the LHS jointly with the HHS nappes has been exhumed at a much faster rate (~ 5 mm/year) along the MBT (Bollinger et al. 2004). Active faulting accompanied by rapid differential tectonic uplift (~ 4–15 mm/year) has also been deciphered along the MFT, from northwestern India to central Nepal (Kumar et al. 2006; Lavé and Avouac 2000; Patel and Manmohan 2020; Wesnousky et al. 1999).

The Himalayan frontal wedge, bounded between the MBT and MFT, is essentially made up of unmetamorphosed to low-grade metamorphosed but strongly deformed Tertiary rocks of the SHS (Fig. 1a). In northwest Himalaya, the MBT is marked by the contact between the Proterozoic LHS and the Cenozoic SHS (Thakur et al. 2010; Valdiya 1984). The MFT, however, is usually not exposed at the surface and identified by the tectonic contact between the Indo-Gangetic alluvium and the late-Cenozoic Siwalik rocks of the SHS (Powers et al. 1998; Thakur 2013). In the presently studied transect of the Himalayan frontal wedge (Fig. 1), the southernmost bounding thrust is marked by the NT (Célérier et al. 2009; Thakur et al. 2010) near Pinjore town, while the northern bounding thrust is the MBT at Gambarpul town. Lithologies between NT and MBT include fluvial sandstone and shallow marine fossiliferous limestone of the Paleogene Subathu and Dagshai formations (Fig. 2a–g). Several slices of the Paleogene Subathu-Dagshai rocks (ca. ~ 41–25 Ma) forming an imbricate structure get exposed within this wedge (Najman and Garzanti 2000). The intermediate major thrusts, progressively from the south are the Bilaspur thrust (BT), the Surajpur thrust (ST), and the Ranon thrust (RT) (Bose et al. 2009). The NW-SE trending NT separates the conglomerate bed of the Neogene Siwalik Group from the overlying sandstone-shale beds of the Paleogene Dagshai Formation (Fig. 1c). The damage zone has a well-developed gouge zone (~ 100 m) containing fragments of calcite veins (Fig. 2a). The MBT is exposed near the Gambarpul area and separates the fossiliferous limestone (Fig. 2e, f) and calcareous siltstone of Paleogene Subathu Formation on its footwall from the overlying predominantly siliciclastic rocks of the LHS of Neo-Proterozoic age (Fig. 1b). Discrete stromatolitic limestone bodies (Fig. 2h) of the Krol Group (ca. ~ 540 Ma) (Dey et al. 2020; Kumar 2020) are present within the dominantly siliciclastic rocks of the Infra-Krol sequence in the hanging wall LHS rocks. The major thrust contacts from NT to MBT are all characterized by the presence of pervasive calcite veins as compared to the rest of the thrust sheet (Fig. 2). The veins show deformation with brecciated nature in NT (Fig. 2a), while in BT, ST, RT, and MBT, they show co-folding with the deformed rocks (Fig. 2b–f). The preferential occurrence of the veins along the major thrust planes and their co-deformation along with the thrust zone rocks prompted us to infer these veins as syn-tectonic veins. The current study focuses on these syn-tectonic calcite veins (Fig. 2a–f) and deformed calcite-bearing limestones (Fig. 2g, h) occurring within the Himalayan frontal wedge bounded between the MBT and the NT.

Ten calcite samples were collected across the thrust splays from NT in the south to MBT in the north. Sampling localities and sample types are given in Supplementary Table 1S. PJ5 was collected from the fragmented calcite veins within the gouge rocks of the NT (Fig. 2a) while PWN1 represents calcite veins from the BT (Fig. 2b) and CM1 is from fossiliferous Subathu limestone in the ST sheet (Fig. 2g). CM2 (Fig. 2c) and KP1 (Fig. 2d) are calcite vein samples collected from a
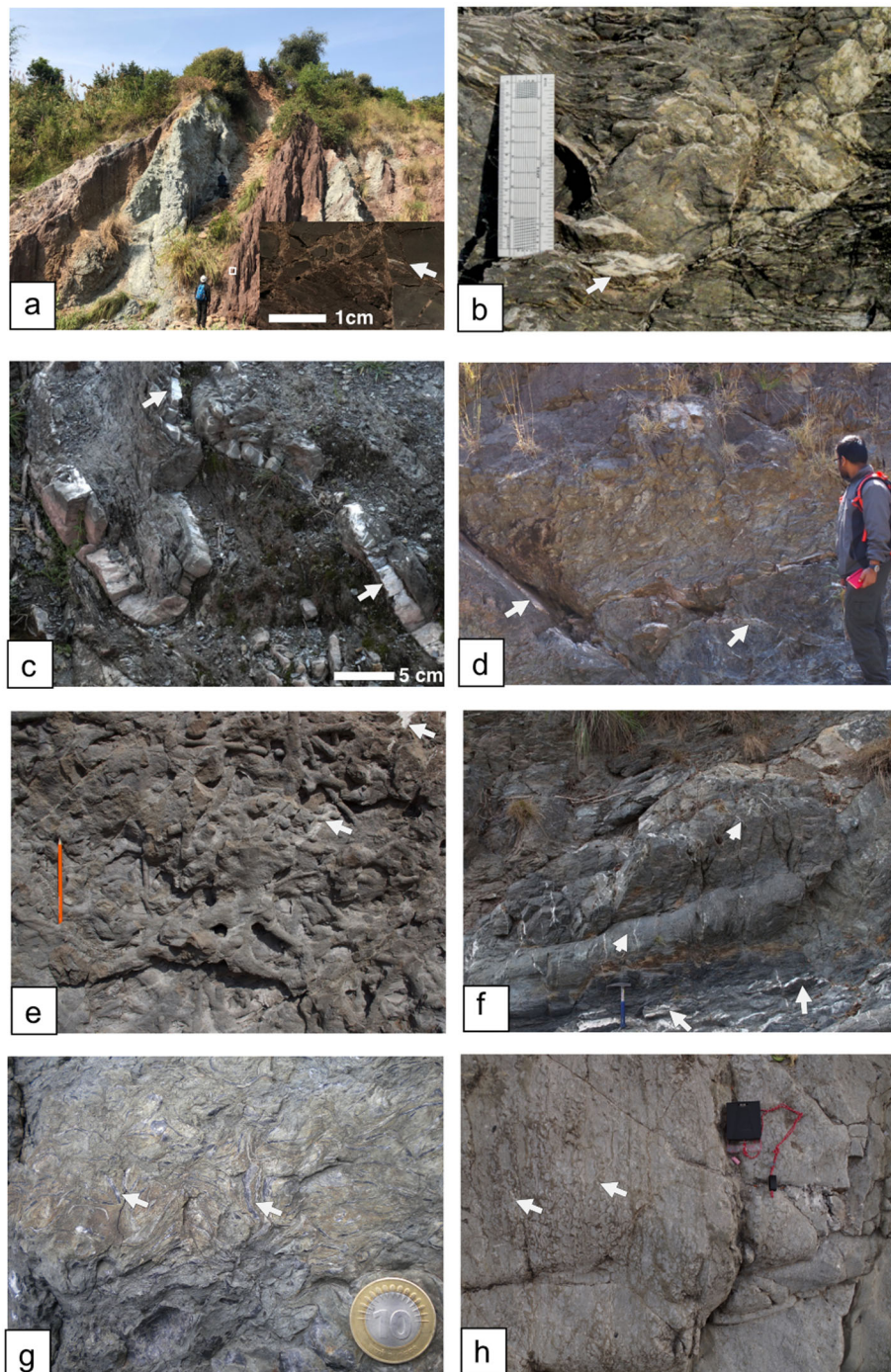
Fig. 2 a The gouge rocks of NT exhibiting fragmented calcite veins (PJ5). The inset shows fragments of calcite vein (arrow) in obtained sample. **b** Folded calcite veins (arrow) (PWN1) occurring in the hanging wall of BT. **c** Co-folded calcite veins (CM2) occurring near a splay thrust of RT. **d** Folded calcite veins (KP1) occurring near deformed rocks of RT. **e** Calcite veins (arrows) within fossiliferous limestones of Subathu Formation in footwall of MBT. **f** Folded and deformed calcite veins (long arrows) (GM8) within the calcareous shale and limestone alternation of Subathu Formation occurring in footwall of MBT. The narrow dilational veins (short arrow) (GM8a) are of older generation. **g** Fossiliferous limestone of Subathu formation (CM1) showing well preserved fossils (arrows). **h** Stromatolitic limestone (GM5l) (arrows show lining of stromatolite layers) of Krol Formation, occurs as discrete bodies within the hanging wall of MBT

splay thrust in the RT sheet and RT respectively. Samples GM8, GM6a were collected from thrust-related foliation-parallel calcite veins (Fig. 2e, f) within the foot-wall block of the MBT while GM8a was from an older dilatational vein truncated by thrust-related foliation at the same site. GM4 and GM5I were collected from the MBT hanging wall stromatolitic limestone of the Krol Group (Fig. 2h).

3 Methodology

3.1 Microstructural studies

The microstructural studies of the calcite samples were performed on polished thin sections using a polarizing microscope. Additionally, the crystallographic preferred orientation (CPO) maps of the calcite grains were obtained using the Nordlys electron backscattered diffraction (EBSD) detector attached to a scanning electron microscope (SEM) JEOL JSM6390A at Hiroshima University. An accelerating voltage of 15 kV and sample tilt of 70° was used for the EBSD analyses. The EBSD patterns were indexed using HKL Channel 5.0 software package. Automatic detection of the center of 6–12 Kikuchi bands using the Hough transform routine (Adams et al. 1993) was followed by comparing the obtained solid angles from the patterns with HKL calcite match unit containing 60 reflectors to index the pattern. Usage of a smaller number of bands was not preferred

since it drastically increases the amount of systematic mis-indexing (Bestmann and Prior 2003).

3.2 Clumped isotope analysis

The isotope analyses ($\delta^{13}C$, $\delta^{18}O$, and Δ_{47}) of all the carbonate samples were measured at Kyushu University, Japan in two sets. The first set (SET 1) of samples were analyzed in December 2018 while the second set (SET 2-1 and 2-2) from September to October 2019 (Table 1 and Supplementary Table 2S). In the present study, the samples were prepared and analyzed by the same method as mentioned in Kato et al. 2019. The powdered calcite specimens of 6–9 mg were digested by 105% phosphoric acid at 90 °C (within 10 min), and the generated CO_2 was trapped immediately and dehydrated using liquid nitrogen and ethanol slush in a stainless-steel vacuum line. The dehydrated CO_2 was removed of all organic contaminants, by passing with helium gas through a 30-m-long capillary column (Supel-Q PLOT) cooled at − 10 °C. Purified CO_2 was then analyzed by dual inlet mass spectrometer (Finnigan MAT-253) configured for measurements of masses 44–49 with pressure adjustment that produced an m/z 44 signal of 16 V. The pressure baseline (PBL) correction (He et al. 2012) with the off-peak measurement of the background intensities of masses 45–49 was also applied. Each analysis includes 4–8 sets of measurement sequences that consist of 4.5

Table 1 Calcite clumped isotope temperatures of the samples. (Raw data of the analysis is in Supplementary Table 2S)

		$\delta^{13}C$	$\delta^{18}O$	$\Delta_{47\text{-}ARF}$	(°C)	Δ_{47} Temperature	
		(‰ VPDB)	(‰ VPDB)	(‰) SE		Max	Min
SET 1	PJ5	− 10.91	− 15.63	0.470 ± 0.009	170.8	182.7	159.8
	GM8a	− 6.36	− 12.26	0.475 ± 0.008	164.4	174.7	154.8
	GM6a	− 8.74	− 13.39	0.416 ± 0.008	257.6	274.2	242.4
	GM4	2.69	− 13.97	0.413 ± 0.016	262.5	300.4	231.2
SET 2-1	PWN1	− 6.48	− 14.43	0.418 ± 0.011	251.6	274.8	231.2
	CM1	− 2.99	− 8.40	0.516 ± 0.010	122.9	131.6	114.8
	CM2	− 6.25	− 14.11	0.423 ± 0.007	242.1	255.9	229.3
	KP1	− 7.08	− 13.18	0.423 ± 0.008	243.5	260.1	228.3
	GM8	− 6.15	− 12.38	0.421 ± 0.009	246.2	266.0	228.4
	GM6a	− 9.02	− 13.19	0.419 ± 0.012	250.7	276.2	228.5
	GM5I	6.12	− 10.06	0.410 ± 0.011	269.4	296.7	245.8
SET 2-2	PWN1	− 6.48	− 14.36	0.413 ± 0.006	263.3	275.8	251.6
	CM1	− 2.98	− 8.34	0.521 ± 0.010	118.1	126.9	110.0
	CM2	− 6.28	− 14.21	0.400 ± 0.035	292.6	412.4	219.5
	KP1	− 7.17	− 13.08	0.412 ± 0.010	266.0	290.1	244.7
	GM8	− 6.23	− 12.53	0.424 ± 0.007	239.8	253.8	226.9
	GM6a	− 9.09	− 13.21	0.428 ± 0.011	233.1	255.2	213.5
	GM5I	6.14	− 10.12	0.435 ± 0.014	221.6	246.6	199.8

off-peak cycles, 8 on-peak cycles, and 4 off-peak cycles. The total analysis time was 2–4 h. Measured intensities of masses 45–49 were processed to calculate $\delta^{13}C$ and $\delta^{18}O$ with Isodat, in which an abundance of ^{17}O was calculated with ^{17}O correction (Brand et al. 2010).

The Δ_{47} value against working gas (Oztech; $\delta^{13}C$ = – 3.62‰ VPDB, and $\delta^{18}O$ = 25.04‰ VSMOW) was obtained. The raw Δ_{47} values from equilibrated against working gases ($\Delta_{47\text{-}[EGvsWG]}$) was initially corrected using the slope of Δ_{47}-dependence (– 0.000064‰ in Δ_{47} per 1‰ of δ^{47}; Kato et al., 2019). The Δ_{47} values were then converted to a reference frame ($\Delta_{47\text{-RF}}$) by an empirical transfer function and finally converted to the absolute reference frame (ARF) (Dennis et al. 2011) $\Delta_{47\text{-ARF}}$ by adding the acid fractionation factor (Defliese et al. 2015). We constructed the empirical transfer function using $\Delta_{47\text{-}[EGvsWG]}$ values of equilibrated CO_2 gases (at 4 and 60 °C) and heated CO_2 gases (at 1000 °C) as follows.

$$\Delta_{47-RF} = 1.004108 \cdot \Delta_{47-[EGvsWG]}(\Delta_{47-corrected}) + 1.043887 \left(R^2 = 0.9994\right) \quad (1)$$

Finally, the substitution of the acid correction 0.082‰ at 90 °C (Defliese et al. 2015) yielded $\Delta_{47\text{-ARF}}$ values of the analyzed samples.

The stability and reliability of Δ_{47} measurements were confirmed by the analyses of an in-house standard (Kato et al. 2019) (Hiroshima standard [Solhofen limestone], $\delta^{13}C$ = – 0.47‰ and $\delta^{18}O$ = – 5.04‰). The inter-measurement deviation of Δ_{47} values was 0.0108‰ (1σ, v=12) during the period of sample measurements.

In this study, to convert Δ_{47} values to absolute temperatures (T), we applied the following Δ_{47}-temperature calibration based on measurements of synthesized calcites reported in Kato et al. (2019).

$$\Delta_{47} = (0.0354 \pm 0.0013) * 10^6 / T^2 + (0.290 \pm 0.015) \quad (2)$$

4 Results and discussion

4.1 Calcite twin morphologies and EBSD analysis

Calcite e-twin morphology and width have been correlated with deformation temperatures in experiments to obtain a standard of comparison which can be used for estimating deformation temperatures from naturally deformed calcites (Burkhard 1993; Ferrill et al. 2004; Ferrill and Groshong 1993; Lacombe 2010; Rowe and Rutter 1990). Typically, four types of calcite deformation twins have been reported depending on twin width and morphologies (Ferrill et al. 2004). Type-I twins (width < 3 μm) are dominant at deformation temperatures below 170 °C and occur as straight lines. Type-II, Type-III, and Type-IV twins have width > 3 μm and dominate above 200 °C. Morphologically, Type-II occurs as tabular thick

twins, while Type-III and Type-IV exhibit curved (or lensoid) and thick patchy twins, respectively.

In the studied samples, calcite has variable grain size (2 mm–100 μm) and the observations of twin morphology (Fig. 3) in the optical microscope and misorientation data from SEM-EBSD (Fig. 4) confirm the development of deformation e-twins. PJ5 shows the development of predominantly one set of Type-I twins, with few minor grains showing two sets of Type-I twins (Fig. 3a). PWN1 (Fig. 3b) and GM8a (Fig. 3f) show the development of one set and two sets of Type-I twins with few grains developing Type-II twins. Samples CM2 and KP1 (Fig. 3c, d) show predominant development of Type-II twins. GM6a shows the development of both Type-II and Type-III twins (Fig. 3e). CM1, the fossiliferous limestone, shows the limited development of twins (Fig. 3g). Fine-grained recrystallized calcite in GM4 and GM5I show weakly developed Type-II twins (Fig. 3h).

For SEM-EBSD grain size orientation analysis, the step size of 2 μm and 3 μm were used, which being much smaller than the average calcite grain size reduces the possibility of mis-indexing. However, such a step size reduces the probability of mapping Type-I twins (< 3 μm). Hence, EBSD maps of PJ5, PWN1, and CM1 were not obtained. The inverse pole figure (IPF) coloring of the maps of GM6a and GM8a (Supplementary Fig. 1S) displays the individual grain orientations in relation to the crystallographic axis as shown in the IPF key. The band contrast maps (Supplementary Fig. 1S) represent surface damage and misorientation boundaries and can be used to verify the reliability of the orientation maps. Misorientation angle distributions are represented in Fig. 4. The random pair misorientation angle distributions vary from the theoretical curve for random orientation distribution (Fig. 4a–d). The neighbor-pair misorientation angle distributions for the samples show a distinctive peak at about 75°–80° confirming development of e-twins in calcite grains. In this context, the dominance of Type-I twins in PJ5, CM1, and GM8a suggests a lower temperature of deformation ($\sim$ 170 °C) for these samples while the presence of thicker Type-II and curved Type-III deformation twins in sample PWN1, CM2, KP1, and GM6a suggests a higher temperature (> 200 °C) of deformation. The limited development of Type-II twins in GM4 and GM5I indicates the possibility of deformation temperature > 200 °C.

4.2 Clumped isotope thermometry: validity and future applicability in studying fault zone rocks

Table 1 shows the isotope analyses of the vein and diagenetic calcite samples from the Subathu-Dagshai (samples PJ5, PWN1, CM1, CM2, KP1, GM6a, GM8a, and GM8 and Krol (samples GM4 and GM5I) formations.
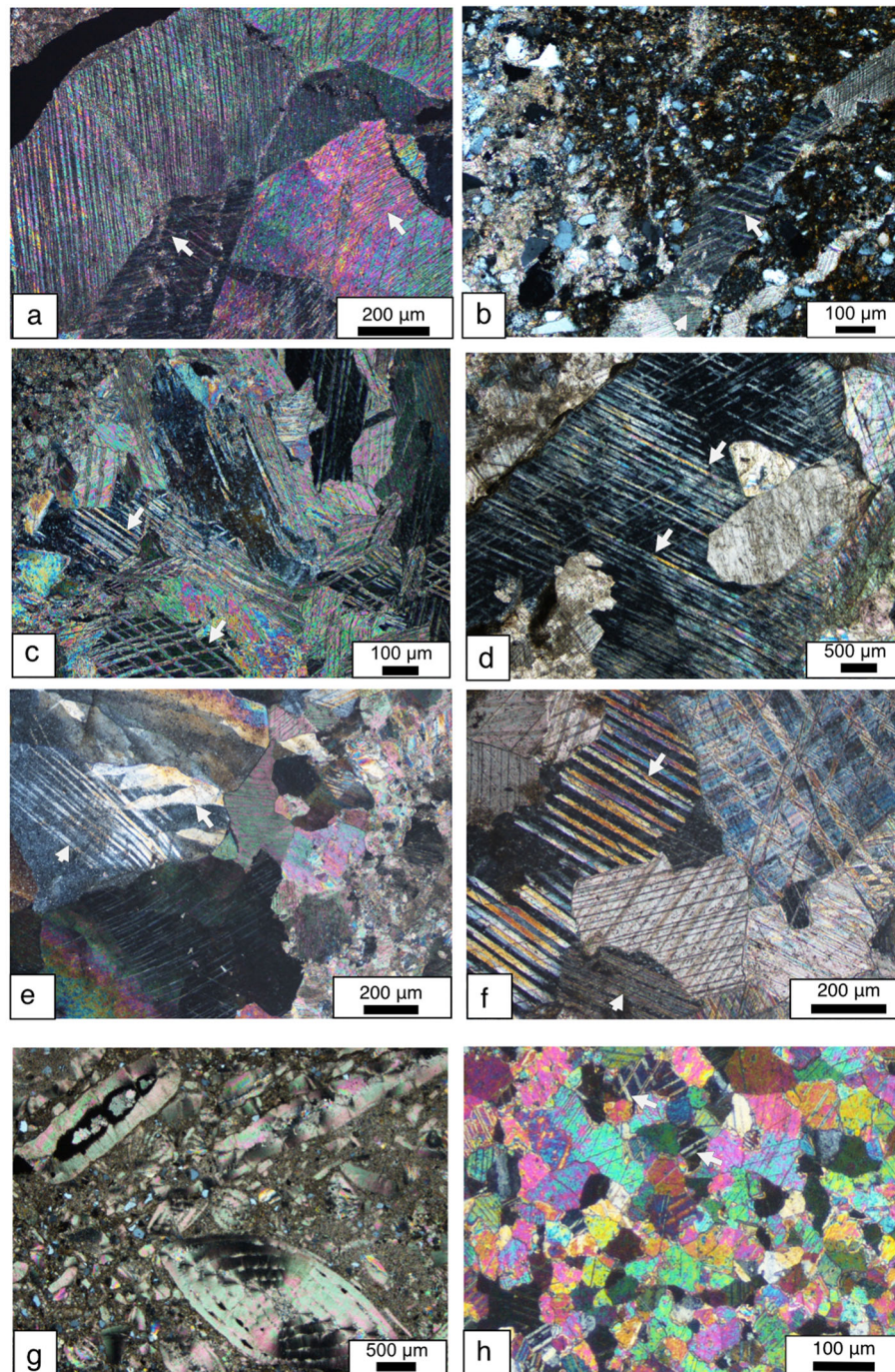
Fig. 3 a Type-I deformation twins (arrows) have predominantly developed within calcites veins from the gouge of NT (PJ5), implying a temperature of less than 170 °C (Ferrill et al. 2004). **b** Limited development of type-I and type-II twins in the calcite veins of PWN1. **c** Predominance of type-II twins in the calcite veins of CM2. **d** Predominance of type-II twins in the calcite veins of KP1. **e** Type-II (short arrow) and type-III (long arrow) twins with few recrystallized calcite grains (small grains in the left side) occur within footwall calcite veins near MBT contact (GM6a). **f** Type-I deformation twins (short arrow) have predominantly developed in the older dilational calcite veins occurring in limestones (GM8a) in footwall of MBT. Few grains have developed type-II twins (long arrow). **g** Fossiliferous limestone sample CM1 showing foraminifera fossils with limited deformation twins. **h** Few twins (arrows) are developed in the fine-grained stromatolitic bodies occurring in the hanging wall of MBT (GM5l)
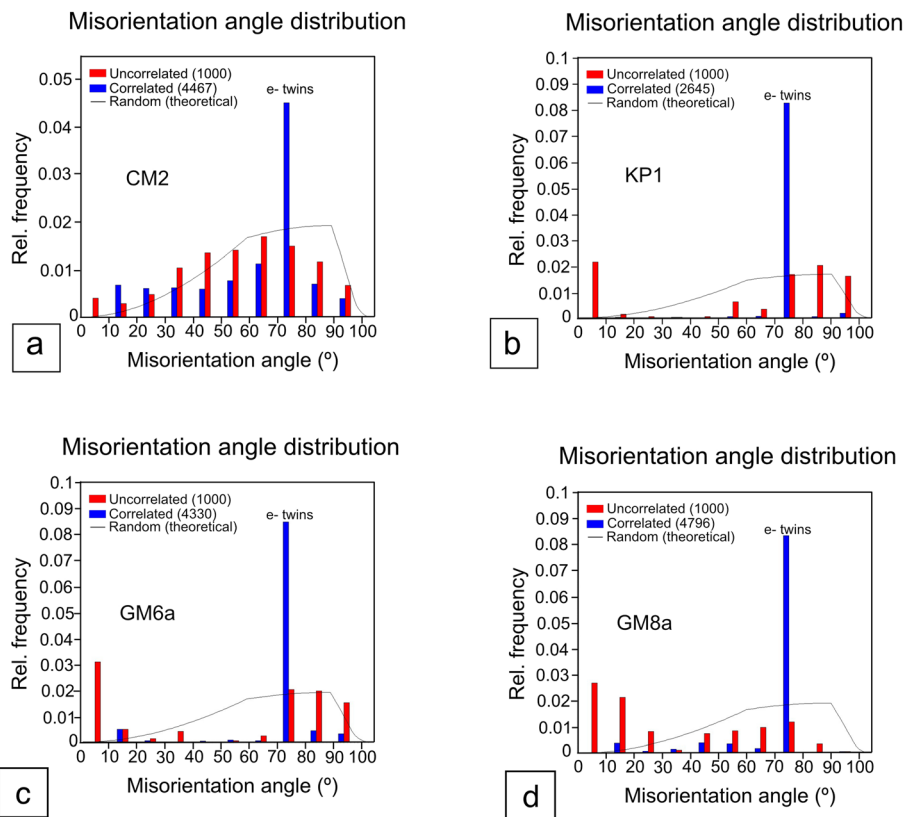
Fig. 4 Misorientation angle distribution plot of representative samples. Both neighbor-pair/correlated (blue) and random-pair/uncorrelated (red) are plotted. The theoretical distribution of misorientations (shown by line graph) for calcite is also plotted. **a** CM2. **b** KP1. **c** GM6a. **d** GM8a. The peaks of neighbor pair misorientation in both the plots suggest development of the e-twins

4.2.1 Subathu and Dagshai formations

The Δ_{47} values, obtained from the vein samples of Subathu and Dagshai formations, vary between 0.400 ± 0.035 and 0.475 ± 0.008‰ corresponding to temperatures 292.6 °C and 164.4 °C. The Δ_{47} value of diagenetic sample CM1 is 0.521 ± 0.010‰ corresponding to the temperature 118.1 °C (SET2-2, Table 1). The clumped isotope temperature obtained from the vein samples is ~ 50–170 °C higher as compared with the temperature of the diagenetic sample.

4.2.2 Krol Formation

The samples from the Krol Formation (samples GM4 and GM5I) are all diagenetic samples from the stromatolitic limestone. The Δ_{47} values range between 0.435 ± 0.014 and 0.413 ± 0.016‰ corresponding to temperatures 221.6 °C and 262.5 °C. The clumped isotope temperature obtained from the diagenetic samples (GM4 and GM5I) of the Krol Formation is ~ 100–150 °C higher than the diagenetic sample (CM1) of Subathu-Dagshai formations.

4.2.3 Applicability of Δ_{47} thermometry

During cooling from high temperature, Δ_{47} values in calcite have been shown to follow solid-state bond reordering till it reaches the blocking temperature of calcite (~ 150–200 °C), where the Δ_{47} value gets locked (Passey and Henkes 2012; Stolper and Eiler 2015). Calcite residing in the subsurface at high temperature (ca. > 100 °C) for a long period (ca. > 100 Ma) is susceptible to solid-state bond reordering (Bristow et al. 2011; Passey and Henkes 2012; Stolper and Eiler 2015). Therefore, higher apparent temperatures can be preserved through faster cooling/exhumation rates of calcite-bearing rocks (Bristow et al. 2011; Passey and Henkes 2012; Shenton et al. 2015; Stolper and Eiler 2015). In shallow crustal fold-thrust belts, ambient deformation temperatures in fault zones may be high enough (ca. ~ 200 °C) to initiate clumped isotope bond reordering in calcite-bearing rocks as well as syn-tectonic calcite veins. However, the established chronology of thrust movements in the Himalayan fold-thrust belt (FTB) (ca. ~ 10 Ma for MBT to ~ 2 Ma for MFT) (Burbank et al. 1996; Kumar et al.
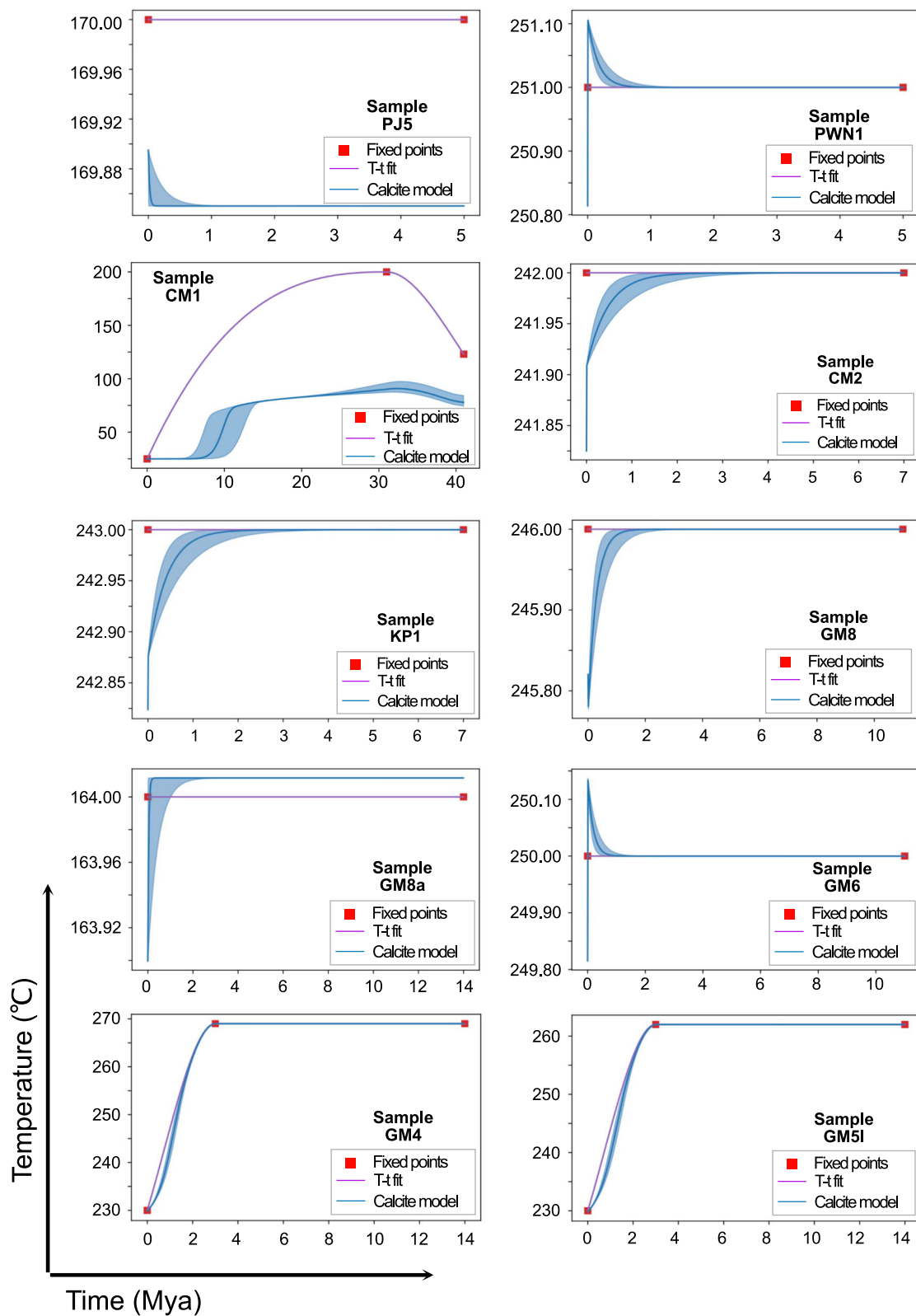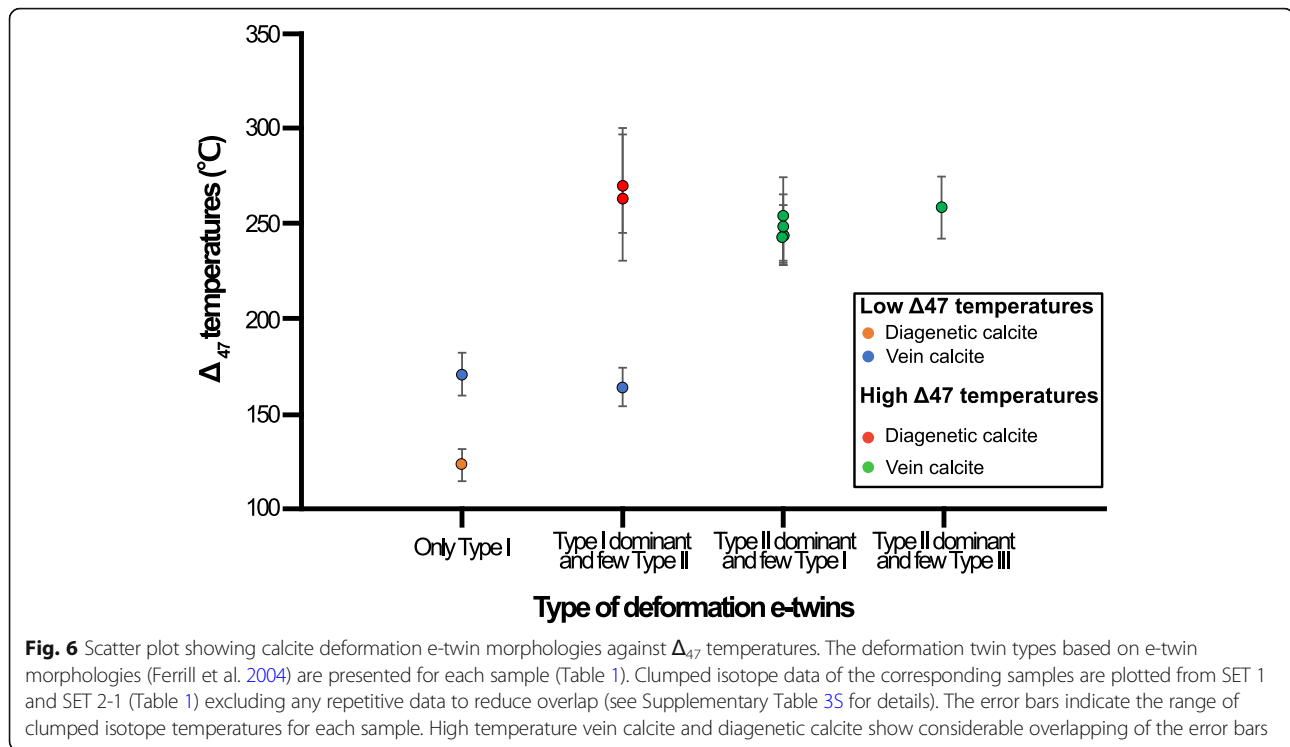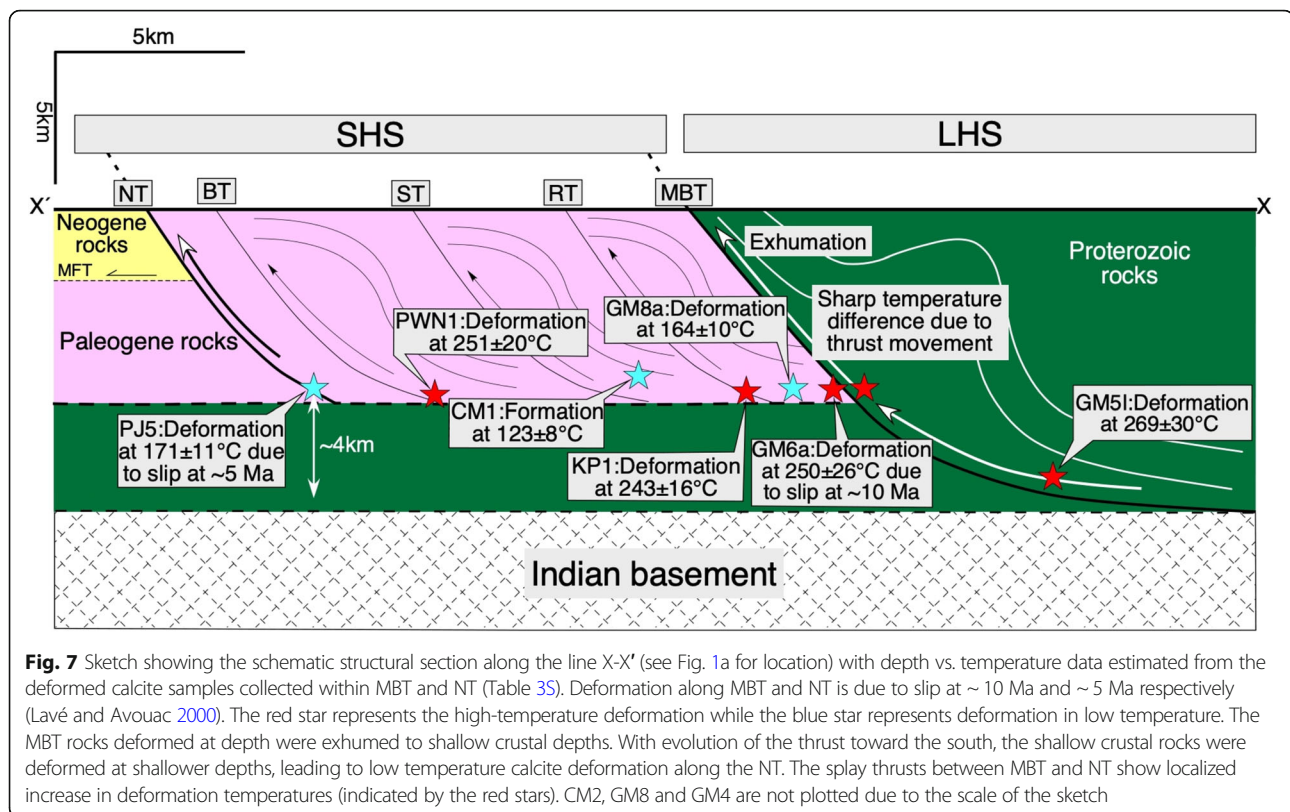
Fig. 5 THRMs (thermal history reordering models) obtained for each sample are shown here. The sample numbers are mentioned in each of the plots. The blue shaded region in each of the plots show the standard error for each generated model, while temperature obtained from clumped isotope thermometry are shown as fixed points and a best fit line is drawn. For additional temperature details, see Supplementary Table 3S

Fig. 6 Scatter plot showing calcite deformation e-twin morphologies against Δ_{47} temperatures. The deformation twin types based on e-twin morphologies (Ferrill et al. 2004) are presented for each sample (Table 1). Clumped isotope data of the corresponding samples are plotted from SET 1 and SET 2-1 (Table 1) excluding any repetitive data to reduce overlap (see Supplementary Table 3S for details). The error bars indicate the range of clumped isotope temperatures for each sample. High temperature vein calcite and diagenetic calcite show considerable overlapping of the error bars

2006; Lavé and Avouac 2000; Meigs et al. 1995; Sangode and Kumar 2003; Sapkota et al. 2013) is on the much lower side of the required time for calcite solid-state bond reordering to be effective. The intermediate thrust faults namely, RT, ST, BT, and NT are also relatively young (< 10 Ma to > 2 Ma) for calcite solid-state bond reordering to be effective. Additionally, the exhumation rate in the last 7 Ma is 1 mm/year in most places (Clift et al. 2008; Lang et al. 2016; Najman et al. 2009; Turab et al. 2017) to as fast as 6–7 mm/year in the North Himalayan Gneissic Domes (Yin 2006). Hence, the analyzed calcite samples from thrust-related veins which experienced the deformation-exhumation path after crystallization would in all probability preserve the deformation temperature as deduced from measured Δ_{47} values. The limestone samples from the Subathu Formation of the SHS (ca. ~ 41 Ma) or the Krol Group of the LHS (ca. ~ 540 Ma), on the contrary, are much older and must have followed a protracted burial or low-T metamorphism-exhumation path after their formation at near-surface environments (ca. ~ 25–30 °C) (Eiler 2011) and might be susceptible to solid-state calcite bond reordering (Dennis and Schrag 2010; Lawson et al. 2018).

The majority of the studied samples (seven out of ten) belong to the vein-calcite category having little residence time after crystallization for thermal resetting of clumped isotope temperatures to be effective. However, to evaluate the degree of bond reordering, the thermal history reordering models "THRMs" (as defined in Shenton et al. 2015) for all the samples were generated using the ClumpyCool package (Lloyd et al. 2017) as presented in Supplementary Table 3S and Fig. 5. Calcite reordering parameters are from Stolper and Eiler (2015) that uses the CDES25-temperature calibration. While running THRMs, the initialization (Time 0) was taken as the precipitation age of the calcite. For vein samples, the precipitation age was considered to be synchronous with slip on individual thrust planes with which the veins are associated. For the limestone samples, the precipitation age is the age of deposition of the stratigraphic units from which the samples were collected (Supplementary Table 3S). For the latter samples, the temperature of burial was assumed to be ca. ~ 230 °C—the maximum burial temperature experienced by the LHS rocks (Colleps et al. 2018; Yu 2014). The calcite e-twin based palaeothermometry data were used as the temperature of deformation for all the samples. The generated THRMs (Fig. 5) for the samples indicate that bond reordering did not take place in the vein samples but might have occurred for the diagenetic samples (CM1, GM4, and GM5I). Hence, the Δ_{47}-based apparent temperatures of the samples (Table 1 and Supplementary Table 2S) could be interpreted to represent either the calcite precipitation temperature (for the syn-tectonic calcite veins) or the temperature of deformation-metamorphism of the calcite-bearing rocks (as this was the last high-

Fig. 7 Sketch showing the schematic structural section along the line X-X' (see Fig. 1a for location) with depth vs. temperature data estimated from the deformed calcite samples collected within MBT and NT (Table 3S). Deformation along MBT and NT is due to slip at ~ 10 Ma and ~ 5 Ma respectively (Lavé and Avouac 2000). The red star represents the high-temperature deformation while the blue star represents deformation in low temperature. The MBT rocks deformed at depth were exhumed to shallow crustal depths. With evolution of the thrust toward the south, the shallow crustal rocks were deformed at shallower depths, leading to low temperature calcite deformation along the NT. The splay thrusts between MBT and NT show localized increase in deformation temperatures (indicated by the red stars). CM2, GM8 and GM4 are not plotted due to the scale of the sketch

temperature event to reset the calcite isotopic ratios). In other words, the apparent temperatures obtained from the vein and the whole rock samples indicate the deformation temperatures along the successive thrust slices in the studied transect. It is pertinent here to mention that the apparent temperatures obtained from Δ_{47} data are within the range of the temperature data estimated from the development of the e-twin morphology of the samples (Fig. 6 and Table 3S). Thus, both the conventional e-twin related temperature estimates and clumped isotope thermometry data from the same set of samples are in good agreement suggesting the validity of the interpretation that the Δ_{47}-based apparent temperatures truly represent the deformation temperature of the rocks. It further points to independent future application potentiality of the latter method in low-grade calcite-bearing rocks, provided the calcite samples were not subjected to complete bond reordering.

We also find that Δ_{47}-based deformation temperatures of most of the fault zone samples (excluding the one from NT, or those from the footwall blocks of MBT, see Table 1) are ~ 40–65 °C higher than the temperature commonly observed in slowly exhumed metamorphic rocks (Passey and Henkes 2012; Stolper and Eiler 2015). This discrepancy in the deformation temperature data from the studied transect might be explained if we

assume that thrust-related exhumation in the Himalayan FTB is sufficiently rapid to effectively quench the deformation temperature (Bristow et al. 2011; Passey and Henkes 2012; Stolper and Eiler 2015). The well-documented high exhumation rates of the Himalayan frontal fold-thrust belt (Bollinger et al. 2004; Colleps et al. 2018; Gavillot et al. 2018; Kumar et al. 2006; Lavé and Avouac 2000; Patel and Manmohan 2020; Webb et al. 2011; Wesnousky et al. 1999) bear testimony to the above interpretation.

Thus, in concert with the above lines of evidence, it can be reasonably assumed that the temperatures estimated from Δ_{47} data (Table 1 and Supplementary Table 2S) from the samples reflect deformation temperatures (and hence the depth) at which the slip events occurred during the growth of the Himalayan frontal wedge (Chen et al. 2019; Lacroix and Niemi 2019; Passey and Henkes 2012; Ryb et al. 2017; Shenton et al. 2015; Stolper and Eiler 2015). However, CM1 not being in close vicinity to any of the thrusts might reflect the maximum burial temperature (123 ± 8° C) of the Subathu limestone (Henkes et al. 2013; Shenton et al. 2015). Additionally, the higher temperature (269 ± 30 °C) of the stromatolitic limestone in the hanging wall of MBT might also reflect the burial temperature of the stromatolitic limestone (Colleps et al. 2018; Yu 2014).

The current results are consistent with a general inverted thermal gradient from the structurally higher MBT to the lower-lying NT, which is in conformity with similar inverted thermal gradients documented from a number of transects across the major thrust zones in the Himalayas (Anczkiewicz et al. 2014; Bollinger et al. 2004; Chakraborty et al. 2016; Srivastava and Mitra 1996). The present data show a peak temperature of 269 ± 30 °C at the MBT hanging wall (Fig. 7) (samples GM4, GM5I). The vein samples from the footwall of MBT (Fig. 7) also show Δ_{47} temperature of 250 ± 26 °C (samples GM6a and GM8). Only the sample GM8a show lower temperature (164 ± 10 °C) and may be an older dilational vein that had undergone partial reordering. The samples (samples KP1, CM2, PWN1) occurring at the hanging walls of the intermediate splay thrusts (RT, ST, BT) between MBT and NT (Fig. 7), also, show consistent elevated temperatures (242 ± 13–251 ± 20 °C) which drops to a lower value (171 ± 11 °C) approaching NT hanging wall (Fig. 7) (sample PJ5). Thus, if the overall temperature variation over a longer distance (MBT to NT) is considered, more realistic values of an inverted thermal gradient can be obtained.

We broadly constrain the crustal depths, at which the studied fault zone samples were deformed, by combining the presently generated clumped isotope palaeothermometry data with the previously published estimates of geothermal gradients in the Himalayan FTB. Previous workers estimated a geothermal gradient of 18–24 °C km^{-1} from SHS rocks of the NW Himalaya (Agarwal 1994; van der Beek et al. 2006) while recent works in Sikkim, Arunachal Pradesh of NE Himalaya have documented a geothermal gradient of 22–26 °C km^{-1} from the LHS rocks (Anczkiewicz et al. 2014; Clarke et al. 2016). Thus, a crustal geothermal gradient of 25 °C km^{-1} (Priestley et al. 2008; Sheehan et al. 2013) for the presently studied transect is considered reasonable in light of the existing data. Utilizing the assumed value of geothermal gradient along with the presently generated deformation temperature data (Table 1), the depth of formation of the fault zone rocks were deduced to be ~ 6–7 km and ~ 10–11 km, respectively for the NT and MBT (Fig. 7). In the presently studied part of the Himalayan frontal thrust belt, the observed height difference is ~ 1000 m between the actual outcrop-scale occurrences of the two successive thrust planes (NT and MBT at Pinjore and Gambarpul respectively) and ~ 4 km depth variation deduced from the two zones. Considering the rate of erosion to be constant over the distance of ~ 15 km and the suggested difference in time of formation of ~ 5 Ma (Mishra and Mukhopadhyay 2012) for the NT and MBT, an average exhumation rate of ~ 1 mm/year (Clift et al. 2008; Lang et al. 2016; Najman et al.

2009; Turab et al. 2017) is obtained for the frontal thrust wedge in NW Himalaya. Apart from the peak exhumation rate of ~ 40 mm/year at 55–50 Ma in western Himalaya, the presently obtained exhumation rate is similar to the average rate for the last 7 Ma, which is 1 mm/year in most places to as fast as 6–7 mm/year in the North Himalayan Gneissic Domes (Yin 2006).

The data presented here demonstrate the applicability of the new calcite-based geothermometer refining our ability to reconstruct temperature profile across major faults in an active orogenic setting relying on the carbonate minerals only. In this context, it is important to note that carbonate minerals in limestones as well as in syn-tectonic calcite veins are a dominant constituent of shallow to mid-crustal fault rocks in most of the orogenic belts worldwide. Therefore, the Δ_{47} thermometry technique would be particularly useful in unmetamorphosed to low-grade metamorphosed terrains where conventional thermometers based on element partitioning in metamorphic minerals are inutile. The Δ_{47} thermometry could also act as a preferred mechanism over illite or carbon-based thermometry (Bollinger et al. 2004) from low-grade terrains due to greater availability (than carbonaceous rocks) and lesser analytical complexity (than illite thermometer). Even combining conventional metamorphic mineral-based techniques with the presently practiced calcite clumped isotope thermometry may offer additional significant insights from interior parts of the orogens exposing deeper crustal sections and having experienced greater hydrothermal activity.

5 Conclusion

The calcite e-twin morphologies, as well as clumped isotope data, show great consistency in determining temperatures from the studied fault rocks. The syn-tectonic nature of the veins indicates the temperatures estimated are representative of deformation temperatures. The lower deformation temperature of NT rocks indicates a shallower origin while the higher deformation temperature from MBT rocks implies their deeper origin. The present study suggests the applicability of Δ_{47} thermometry of calcite for estimating deformation temperatures of geologically younger (< 10 Ma) calcite bearing faults, in addition to estimating the cooling history of rocks as reported by other researchers (Chen et al. 2019; Dennis and Schrag 2010; Lawson et al. 2018). The variation of deformation depth for the NT and MBT might help in correlating future studies on deformation microstructures to crustal depths in the context of the Himalayas. Also, the precise estimation of exhumation rates from orogenic belts will require more robust fault-slip chronometric data used in conjunction with clumped isotopic data.

6 Supplementary Information

The online version contains supplementary material available at https://doi.org/10.1186/s40645-021-00435-6.

Additional file 1: Figure 1S. Representative samples showing EBSD mapping areas. (a)-(b) GM6a showing IPF (Inverse Pole Figure) coloring (a) and band contrast (b) maps. (c)-(d) GM8a showing IPF coloring (c) and band contrast (d) maps.

Additional file 2: Table 1S. GPS location (WGS84) and type of the calcite samples.

Additional file 3: Table 2S. Raw data of Δ_{47} thermometry.

Additional file 4: Table 3S. Thermal history data of the analyzed calcite samples.

Authors' contributions
DPS has jointly conducted the fieldwork with JA, GG, and KD, and collected carbonate samples for analysis. The major microstructural analysis including EBSD and the initial sample preparation for clumped isotope analysis were conducted in Hiroshima University, Japan by DPS, JA, and KD. AK and HK have jointly conducted clumped isotopic analysis at Kyushu University, Japan. All the authors were actively involved in shaping the discussion section. The author(s) read and approved the final manuscript.

Availability of data and materials
All the relevant datasets have been provided as a part of supplementary materials with the submitted manuscript.

Declarations

Competing interests
The authors declare that they have no competing interests.

Author details
[1]Department of Earth and Planetary Systems Science, Hiroshima University, Hiroshima 739-8526, Japan. [2]Hiroshima Institute of Plate Convergence Region Research, Hiroshima University, Hiroshima 739-8526, Japan. [3]Department of Earth and Planetary Science, Graduate School of Science, The University of Tokyo, 7-3-1 Hongo, Tokyo 113-0033, Japan. [4]Centre for Advanced Study, Department of Geology, Presidency University, Kolkata 700073, India.

References
Agarwal K (1994) Tectonic evolution of the Almora Crystalline Zone, Kumaun Lesser Himalayas–A reinterpretation. J Geol Soc India 43(1):5–14

Anczkiewicz R, Chakraborty S, Dasgupta S, Mukhopadhyay D, Kołtonik K (2014) Timing, duration and inversion of prograde Barrovian metamorphism constrained by high resolution Lu-Hf garnet dating: a case study from the Sikkim Himalaya, NE India. Earth Planet Sci Lett 407:70–81. https://doi.org/10.1016/j.epsl.2014.09.035

Bestmann M, Prior DJ (2003) Intragranular dynamic recrystallization in naturally deformed calcite marble: diffusion accommodated grain boundary sliding as a result of subgrain rotation recrystallization. J Struct Geol 25(10):1597–1613

Bollinger L, Avouac JP, Beyssac O, Catlos EJ, Harrison TM, Grove M et al (2004) Thermal structure and exhumation history of the Lesser Himalaya in central Nepal. Tectonics 23(5):1–19

Boniface M, Calmels D, Eiler JM, Horita J, Chaduteau C, Vasconcelos C et al (2017) Calibration of the dolomite clumped isotope thermometer from 25 to 350℃, and implications for a universal calibration for all (Ca, Mg, Fe)CO_3 carbonates. Geochim Cosmochim Acta 200:255–279. https://doi.org/10.1016/j.gca.2016.11.028

Bose S, Mandal N, Mukhopadhyay DK, Mishra P (2009) An unstable kinematic state of the Himalayan tectonic wedge: Evidence from experimental thrust-spacing patterns. J Struct Geol 31(1):83–91. https://doi.org/10.1016/j.jsg.2008.10.002

Brand WA, Assonov SS, Coplen TB (2010) Correction for the ^{17}O interference in $\delta(^{13}C)$ measurements when analyzing CO_2 with stable isotope mass spectrometry (IUPAC Technical Report). Pure Appl Chem 82(8):1719–1733

Bristow TF, Bonifacie M, Derkowski A, Eiler JM, Grotzinger JP (2011) A hydrothermal origin for isotopically anomalous cap dolostone cements from south China. Nature 474(7349):68–71

Burbank DW, Leland J, Fielding E, Anderson RS, Brozovic N, Reid MR et al (1996) Bedrock incision, rock uplift and threshold hillslopes in the northwestern Himalayas. Nature 379(6565):505–510

Burkhard M (1993) Calcite twins, their geometry, appearance and significance as stress-strain markers and indicators of tectonic regime: a review. J Struct Geol 15(3–5):351–368. https://doi.org/10.1016/0191-8141(93)90132-T

Célérier J, Harrison TM, Beyssac O, Herman F, Dunlap WJ, Webb AG (2009) The Kumaun and Garwhal Lesser Himalaya, India: Part 2: thermal and deformation histories. Bull Geol Soc Am 121(9–10):1281–1297

Chakraborty S, Anczkiewicz R, Gaidies F, Rubatto D, Sorcar N, Faak K et al (2016) A review of thermal history and timescales of tectonometamorphic processes in Sikkim Himalaya (NE India) and implications for rates of metamorphic processes. J Metamorph Geol 34(8):785–803 https://doi.org/10.1111/jmg.12200

Chakraborty S, Mukhopadhyay DK, Chowdhury P, Rubatto D, Anczkiewicz R, Trepmann C et al (2017) Channel flow and localized fault bounded slice tectonics (LFBST): insights from petrological, structural, geochronological and geospeedometric studies in the Sikkim Himalaya, NE India. Lithos 282–283:464–482. https://doi.org/10.1016/j.lithos.2017.01.024

Chemenda AI, Burg JP, Mattauer M (2000) Evolutionary model of the Himalaya-Tibet system: Geopoem based on new modelling, geological and geophysical data. Earth Planet Sci Lett 174(3–4):397–409

Chen S, Ryb U, Piasecki AM, Lloyd MK, Baker MB, Eiler JM (2019) Mechanism of solid-state clumped isotope reordering in carbonate minerals from aragonite heating experiments. Geochim Cosmochim Acta 258:156–173 https://doi.org/10.1016/j.gca.2019.05.018

Clarke GL, Bhowmik SK, Ireland TR, Aitchison JC, Chapman SL, Kent L (2016) Inverted Oligo-Miocene metamorphism in the Lesser Himalaya Sequence, Arunachal Pradesh, India; age and grade relationships. J Metamorph Geol 34(8):805–820

Clift PD, Hodges KV, Heslop D, Hannigan R, Van Long H, Calves G (2008) Correlation of Himalayan exhumation rates and Asian monsoon intensity. Nat Geosci 1(12):875–880

Colleps CL, McKenzie NR, Stockli DF, Hughes NC, Singh BP, Webb AAG et al (2018) Zircon (U-Th)/He Thermochronometric constraints on Himalayan thrust belt exhumation, bedrock weathering, and cenozoic seawater chemistry. Geochem Geophys Geosyst 19(1):257–271

Cottle JM, Larson KP, Kellett DA (2015) How does the mid-crust accommodate deformation in large, hot collisional orogens? A review of recent research in the Himalayan orogen. J Struct Geol 78:119–133. https://doi.org/10.1016/j.jsg.2015.06.008

Adams BL, Wright SI, Kunze K (1993) Orientation imaging: the emergence of a new microscopy. Metall Trans A 24(4):819–831 https://doi.org/10.1007/BF02656503

Affek HP, Eiler JM (2006) Abundance of mass 47 CO_2 in urban air, car exhaust, and human breath. Geochim Cosmochim Acta 70(1):1–12 https://doi.org/10.1016/j.gca.2005.08.021

DeCelles PG, Gehrels GE, Quade J, Ojha TP (1998) Eocene-early Miocene foreland basin development and the history of Himalayan thrusting, western and central Nepal. Tectonics 17(5):741–765

Defliese WF, Hren MT, Lohmann KC (2015) Compositional and temperature effects of phosphoric acid fractionation on δ47 analysis and implications for discrepant calibrations. Chem Geol 396:51–60

Dennis KJ, Affek HP, Passey BH, Schrag DP, Eiler JM (2011) Defining an absolute reference frame for 'clumped' isotope studies of CO_2. Geochim Cosmochim Acta 75(22):7117–7131. https://doi.org/10.1016/j.gca.2011.09.025

Dennis KJ, Schrag DP (2010) Clumped isotope thermometry of carbonatites as an indicator of diagenetic alteration. Geochim Cosmochim Acta 74(14):4110–4122. https://doi.org/10.1016/j.gca.2010.04.005

Dey S, Dasgupta P, Das K, Matin A (2020) Neoproterozoic Blaini Formation of Lesser Himalaya. Fiction and Fact. GSA Bull, India, pp 1–15

Eiler JM (2007) "Clumped-isotope" geochemistry—the study of naturally-occurring, multiply-substituted isotopologues. Earth Planet Sci Lett 262(3–4): 309–327 https://doi.org/10.1016/j.epsl.2007.08.020

Eiler JM (2011) Paleoclimate reconstruction using carbonate clumped isotope thermometry. Quat Sci Rev 30(25–26):3575–3588. https://doi.org/10.1016/j.quascirev.2011.09.001

Eiler JM, Schauble E (2004) $^{18}O^{13}C^{16}O$ in Earth's atmosphere. Geochim Cosmochim Acta 68(23):4767–4777 https://doi.org/10.1016/j.gca.2004.05.035

Ferrill DA, Groshong RH (1993) Deformation conditions in the northern Subalpine Chain, France, estimated from deformation modes in coarse-grained limestone. J Struct Geol 15(8):995–1006 https://doi.org/10.1016/0191-8141(93)90172-7

Ferrill DA, Morris AP, Evans MA, Burkhard M, Groshong RH, Onasch CM (2004) Calcite twin morphology: a low-temperature deformation geothermometer. J Struct Geol 26(8):1521–1529 https://doi.org/10.1016/j.jsg.2003.11.028

Ferry JM, Passey BH, Vasconcelos C, Eiler JM (2011) Formation of dolomite at 40-80℃ in the Latemar carbonate buildup, Dolomites, Italy, from clumped isotope thermometry. Geology 39(6):571–574 https://doi.org/10.1130/G31845.1

Gavillot Y, Meigs AJ, Sousa FJ, Stockli D, Yule D, Malik M (2018) Late Cenozoic foreland-to-hinterland low-temperature exhumation history of the Kashmir Himalaya. Tectonics 37(9):3041–3068

Ghosh P, Adkins J, Affek H, Balta B, Guo W, Schauble EA et al (2006a) $^{13}C-^{18}O$ bonds in carbonate minerals: A new kind of paleothermometer. Geochim Cosmochim Acta 70(6):1439–1456

Ghosh P, Garzione CN, Eiler JM (2006b) Rapid uplift of the Altiplano revealed through $^{13}C-^{18}O$ bonds in paleosol carbonates. Science 311(5760):511–515 https://doi.org/10.1126/science.1119365

Gibbons AD, Zahirovic S, Müller RD, Whittaker JM, Yatheesh V (2015) A tectonic model reconciling evidence for the collisions between India, Eurasia and intra-oceanic arcs of the central-eastern Tethys. Gondwana Res 28(2):451–492. https://doi.org/10.1016/j.gr.2015.01.001

He B, Olack GA, Colman AS (2012) Pressure baseline correction and high-precision CO_2 clumped-isotope (Δ47) measurements in bellows and micro-volume modes. Rapid Commun Mass Spectrom 26(24):2837–2853 https://doi.org/10.1002/rcm.6436

Henkes GA, Passey BH, Grossman EL, Shenton BJ, Pérez-Huerta A, Yancey TE (2014) Temperature limits for preservation of primary calcite clumped isotope paleotemperatures. Geochim Cosmochim Acta 139:362–382 https://doi.org/10.1016/j.gca.2014.04.040

Henkes GA, Passey BH, Wanamaker AD, Grossman EL, Ambrose WG, Carroll ML (2013) Carbonate clumped isotope compositions of modern marine mollusk and brachiopod shells. Geochim Cosmochim Acta 106:307–325. https://doi.org/10.1016/j.gca.2012.12.020

Hodges KV (2000) Tectonics of the Himalaya and southern Tibet from two perspectives. Geol Soc Am Bull 112(3):324–350. https://doi.org/10.1130/0016-7606(2000)112<324:TOTHAS>2.0.CO;2

Huntington KW, Lechler AR (2015) Carbonate clumped isotope thermometry in continental tectonics. Tectonophysics 647:1–20. https://doi.org/10.1016/j.tecto.2015.02.019

Huntington KW, Saylor J, Quade J, Hudson AM (2015) High late Miocene-Pliocene elevation of the Zhada Basin, southwestern Tibetan Plateau, from carbonate clumped isotope thermometry. Bull Geol Soc Am 127(1–2):181–199

Kato H, Amekawa S, Kano A, Mori T, Kuwahara Y, Quade J (2019) Seasonal temperature changes obtained from carbonate clumped isotopes of annually laminated tufas from Japan: Discrepancy between natural and

synthetic calcites. Geochim Cosmochim Acta 244:548–564 https://doi.org/10.1016/j.gca.2018.10.016

Kluge T, John CM, Jourdan A-L, Davis S, Crawshaw J (2015) Laboratory calibration of the calcium carbonate clumped isotope thermometer in the 25–250 °C temperature range. Geochim Cosmochim Acta 157:213–227 https://doi.org/10.1016/j.gca.2015.02.028

Kumar R (2020) Late Cenozoic Himalayan foreland basin: Sedimentologic attributes. Episodes 43(1):417–428

Kumar S, Wesnousky SG, Rockwell TK, Briggs RW, Thakur VC, Jayangondaperumal R (2006) Paleoseismic evidence of great surface rupture earthquakes along the Indian Himalaya. J Geophys Res Solid Earth 111(3):1–19

Lacombe O (2010) Calcite Twins, a tool for tectonic studies in thrust belts and stable orogenic forelands. Oil Gas Sci Technol – Rev d'IFP Energies Nouv 65(6):809–838 https://doi.org/10.2516/ogst/2009088

Lacroix B, Niemi NA (2019) Investigating the effect of burial histories on the clumped isotope thermometer: an example from the Green River and Washakie Basins, Wyoming. Geochim Cosmochim Acta 247:40–58 https://doi.org/10.1016/j.gca.2018.12.016

Lang KA, Huntington KW, Burmester R, Housen B (2016) Rapid exhumation of the eastern Himalayan syntaxis since the late Miocene. Bull Geol Soc Am 128(9–10):1403–1422

Lavé J, Avouac JP (2000) Active folding of fluvial terraces across the Siwaliks Hills, Himalayas of central Nepal. J Geophys Res Solid Earth 105(B3):5735–5770 https://doi.org/10.1029/1999JB900292

Lawson M, Shenton BJ, Stolper DA, Eiler JM, Rasbury ET, Becker TP et al (2018) Deciphering the diagenetic history of the El Abra Formation of eastern Mexico using reordered clumped isotope temperatures and U-Pb dating. Bull Geol Soc Am 130(3–4):617–629 https://doi.org/10.1130/B31656.1

Lloyd MK, Eiler JM, Nabelek PI (2017) Clumped isotope thermometry of calcite and dolomite in a contact metamorphic environment. Geochim Cosmochim Acta 197:323–344. https://doi.org/10.1016/j.gca.2016.10.037

MacDonald JM, Faithfull JW, Roberts NMW, Davies AJ, Holdsworth CM, Newton M et al (2019) Clumped-isotope palaeothermometry and LA-ICP-MS U–Pb dating of lava-pile hydrothermal calcite veins. Contrib. to. Mineral Petrol 174(7):63 https://doi.org/10.1007/s00410-019-1599-x

Martin AJ (2017) A review of definitions of the Himalayan Main Central Thrust. Int J Earth Sci 106(6):2131–2145 https://doi.org/10.1007/s00531-016-1419-8

McQuarrie N, Ehlers TA (2015) Influence of thrust belt geometry and shortening rate on thermochronometer cooling ages: insights from thermokinematic and erosion modeling of the Bhutan Himalaya. Tectonics 34(6):1055–1079 https://doi.org/10.1002/2014TC003783

Meigs AJ, Burbank DW, Beck RA (1995) Middle-late Miocene (>10 Ma) formation of the Main Boundary thrust in the western Himalaya. Geology 23(5):423 https://doi.org/10.1130/0091-7613(1995)023<0423:MLMMFO>2.3.CO;2

Metcalfe RP (1993) Pressure, temperature and time constraints on metamorphism across the Main Central Thrust zone and High Himalayan Slab in the Garhwal Himalaya. Geol Soc London Spec Publ 74(1):485–509 https://doi.org/10.1144/GSL.SP.1993.074.01.33

Mishra P, Mukhopadhyay DK (2012) Structural evolution of the frontal fold–thrust belt, NW Himalayas from sequential restoration of balanced cross-sections and its hydrocarbon potential. Geol Soc London Spec Publ 366(1):201–228 https://doi.org/10.1144/SP366.6

Mukhopadhyay DK, Mishra P (2005) A balanced cross section across the Himalayan frontal fold-thrust belt, Subathu area, Himachal Pradesh, India: Thrust sequence, structural evolution and shortening. J Asian Earth Sci 25(5):735–746

Najman Y, Bickle M, Garzanti E, Pringle M, Barfod D, Brozovic N et al (2009) Reconstructing the exhumation history of the Lesser Himalaya, NW India, from a multitechnique provenance study of the foreland basin Siwalik Group. Tectonics 29:TC6006 https://doi.org/10.1029/2010TC002778

Najman Y, Garzanti E (2000) Reconstructing early Himalayan tectonic evolution and paleogeography from Tertiary foreland basin sedimentary rocks, Northern India. GSA Bull 112(3):435–449 https://doi.org/10.1130/0016-7606(2000)112<435:REHTEA>2.0.CO;2

Newman J (1994) The influence of grain size and grain size distribution on methods for estimating paleostresses from twinning in carbonates. J Struct Geol 16(12):1589–1601 https://doi.org/10.1016/0191-8141(94)90129-5

Parlangeau C, Dimanov A, Lacombe O, Hallais S, Daniel JM (2019) Uniaxial compression of calcite single crystals at room temperature: Insights into twinning activation and development. Solid Earth 10(1):307–316 https://doi.org/10.5194/se-10-307-2019

Passey BH, Henkes GA (2012) Carbonate clumped isotope bond reordering and geospeedometry. Earth Planet Sci Lett 351–352:223–236. https://doi.org/10.1016/j.epsl.2012.07.021

Patel RC, Manmohan (2020) Mio-Pliocene Tectonics and Exhumation Histories of the NW– and NE–Himalaya. Episodes 43(1):381–403. https://doi.org/10.18814/epiiugs/2020/020024

Powers PM, Lillie RJ, Yeats RS (1998) Structure and shortening of the Kangra and Dehra Dun reentrants, Sub-Himalaya, India. Geol Soc Am Bull 110(8):1010–1027 https://doi.org/10.1130/0016-7606(1998)110<1010:SASOTK>2.3.CO;2

Priestley K, James J, Mckenzie D (2008) Lithospheric structure and deep earthquakes beneath India, the Himalaya and southern Tibet. Geophys J Int 172(1):345–362 https://doi.org/10.1111/j.1365-246X.2007.03636.x

Rowe KJ, Rutter EH (1990) Palaeostress estimation using calcite twinning: experimental calibration and application to nature. J Struct Geol 12(1):1–17 https://doi.org/10.1016/0191-8141(90)90044-Y

Ryb U, Lloyd MK, Stolper DA, Eiler JM (2017) The clumped-isotope geochemistry of exhumed marbles from Naxos, Greece. Earth Planet Sci Lett 470:1–12. https://doi.org/10.1016/j.epsl.2017.04.026

Rybacki E, Evans B, Janssen C, Wirth R, Dresen G (2013) Influence of stress, temperature, and strain on calcite twins constrained by deformation experiments. Tectonophysics 601:20–36. https://doi.org/10.1016/j.tecto.2013.04.021

Saha P, Bose S, Mandal N (2016) Sandbox modelling of sequential thrusting in a mechanically two-layered system and its implications in fold-and-thrust belts. J Geodyn 100:104–114. https://doi.org/10.1016/j.jog.2016.05.005

Sangode SJ, Kumar R (2003) Magnetostratigraphic correlation of the Late Cenozoic fluvial sequences from NW Himalaya, India. Curr Sci 84(8): 1014–1024

Sapkota SN, Bollinger L, Klinger Y, Tapponnier P, Gaudemer Y, Tiwari D (2013) Primary surface ruptures of the great Himalayan earthquakes in 1934 and 1255. Nat Geosci 6(1):71–76 https://doi.org/10.1038/ngeo1669

Schauble EA, Ghosh P, Eiler JM (2006) Preferential formation of ^{13}C-^{18}O bonds in carbonate minerals, estimated using first-principles lattice dynamics. Geochim Cosmochim Acta 70(10):2510–2529 https://doi.org/10.1016/j.gca.2006.02.011

Schultz MH, Hodges KV, Ehlers TA, van Soest M, Wartho JA (2017) Thermochronologic constraints on the slip history of the South Tibetan detachment system in the Everest region, southern Tibet. Earth Planet Sci Lett 459:105–117. https://doi.org/10.1016/j.epsl.2016.11.022

Searle MP, Godin L (2003) The South Tibetan detachment and the Manaslu Leucogranite: a structural reinterpretation and restoration of the Annapurna-Manaslu Himalaya, Nepal. J Geol 111(5):505–523 https://doi.org/10.1086/376763

Sharma R, Villa IM, Kumar S (2019) Crustal architecture and evolution of the Himalaya-Karakoram-Tibet Orogen: introduction. Geol. Soc. London, Spec. Publ. 481(1):1–5 https://doi.org/10.1144/SP481-2019-46

Sheehan AF, de la Torre TL, Monsalve G, Geoffrey AA, Hacker BR (2013) Physical state of Himalayan crust and uppermost mantle: constraints from seismic attenuation and velocity tomography. J Geophys Res Solid Earth 119:567–580 https://doi.org/10.1002/2013JB010601

Shenton BJ, Grossman EL, Passey BH, Henkes GA, Becker TP, Laya JC et al (2015) Clumped isotope thermometry in deeply buried sedimentary carbonates: the effects of bond reordering and recrystallization. Bull Geol Soc Am 127(7–8): 1036–1051 https://doi.org/10.1130/B31169.1

Siman-Tov S, Affek HP, Matthews A, Aharonov E, Reches Z (2016) Shear heating and clumped isotope reordering in carbonate faults. Earth Planet Sci Lett 445:136–145. https://doi.org/10.1016/j.epsl.2016.03.041

Singh RJ, Sharma MK, Ghosh T, Kumar P (2015) Tectonic architecture of the Paleogene belt and adjoining lithostratigraphic units in Parwanoo-Subathu sector of the Himachal Himalaya, India. Indian J Geosci 69(1):31–44

Srivastava P, Mitra G (1996) Deformation mechanisms and inverted thermal profile in the North Almora Thrust mylonite zone, Kumaon Lesser Himalaya, India. J Struct Geol 18(1):27–39 https://doi.org/10.1016/0191-8141(95)00085-R

Stolper DA, Eiler JM (2015) The kinetics of solid-state isotope-exchange reactions for clumped isotopes: a study of inorganic calcites and apatites from natural and experimental samples. Am J Sci 315(5):363–411 https://doi.org/10.2475/05.2015.01

Swanson EM, Wernicke BP, Eiler JM, Losh S (2012) Temperatures and fluids on faults based on carbonate clumped-isotope thermometry. Am J Sci 312(1):1–21 https://doi.org/10.2475/01.2012.01

Thakur VC (2013) Active tectonics of Himalayan Frontal Fault system. Int J Earth Sci 102(7):1791–1810 https://doi.org/10.1007/s00531-013-0891-7

Thakur VC, Jayangondaperumal R, Malik MA (2010) Redefining Medlicott-Wadia's Main Boundary Fault from Jhelum to Yamuna: An active fault strand of the Main Boundary Thrust in northwest Himalaya. Tectonophysics 489(1–4):29–42. https://doi.org/10.1016/j.tecto.2010.03.014

Turab SA, Stüwe K, Stuart FM, Chew DM, Cogne N (2017) Tectonics drives rapid exhumation of the western Himalayan syntaxis: evidence from low-temperature thermochronometry of the Neelum valley region, Pakistan. Lithosphere. 9(6):874–888 https://doi.org/10.1130/L626.1

Valdiya KS (1984) Evolution of the Himalaya. Tectonophysics. 105(3):229–248 https://doi.org/10.1016/0040-1951(84)90205-1

van der Beek P, Robert X, Mugnier JL, Bernet M, Huyghe P, Labrin E (2006) Late Miocene - Recent exhumation of the central Himalaya and recycling in the foreland basin assessed by apatite fission-track thermochronology of Siwalik sediments, Nepal. Basin Res 18(4):413–434

Wang Z, Schauble EA, Eiler JM (2004) Equilibrium thermodynamics of multiply substituted isotopologues of molecular gases. Geochim Cosmochim Acta 68(23):4779–4797 https://doi.org/10.1016/j.gca.2004.05.039

Webb AAG, Schmitt AK, He D, Weigand EL (2011) Structural and geochronological evidence for the leading edge of the Greater Himalayan Crystalline complex in the central Nepal Himalaya. Earth Planet Sci Lett 304(3–4):483–495. https://doi.org/10.1016/j.epsl.2011.02.024

Wesnousky SG, Kumar S, Mohindra R, Thakur VC (1999) Uplift and convergence along the Himalayan Frontal Thrust of India. Tectonics 18(6):967–976 https://doi.org/10.1029/1999TC900026

Yin A (2006) Cenozoic tectonic evolution of the Himalayan orogen as constrained by along-strike variation of structural geometry, exhumation history, and foreland sedimentation. Earth Sci Rev 76(1–2):1–131 https://doi.org/10.1016/j.earscirev.2005.05.004

Yu H (2014) Contractional Tectonics : investigations of ongoing construction of the Himalaya fold-thrust belt and the Trishear model of fault-propagation folding. LSU Doctoral Dissertations 2683. https://digitalcommons.lsu.edu/gradschool_dissertations/2683.

Publisher's Note

Springer Nature remains neutral with regard to jurisdictional claims in published maps and institutional affiliations.